solids

MDPI

Article

Uncovering the Effects of Non-Hydrostaticity on Pressure-Induced Phase Transformation in Xenotime-Structured $TbPO_4$

Jai Sharma and Corinne E. Packard *

Department of Metallurgical and Materials Engineering, Colorado School of Mines, Golden, CO 80401, USA
* Correspondence: cpackard@mines.edu

Abstract: The pressure-induced phase transformations of rare earth orthophosphates ($REPO_4$s) have become increasingly relevant in ceramic matrix composite (CMC) research; however, understanding of the shear-dependence of these transformations remains limited. This study employs diamond anvil cell experiments with three pressure media (neon, KCl, sample itself/no medium) to systematically assess the effect of shear on the phase transformations of $TbPO_4$. Results show a lowering of the $TbPO_4$ transformation onset pressure (P_{onset}) as well as an extension of the xenotime–monazite phase coexistence range under non-hydrostatic conditions. The $TbPO_4$ P_{onset} under no medium (4.4(3) GPa) is the lowest $REPO_4$ P_{onset} reported to date and represents a ~50% drop from the hydrostatic P_{onset}. Enthalpic differences likely account for lower P_{onset} values in $TbPO_4$ compared to $DyPO_4$. Experiments also show scheelite may be the post-monazite phase of $TbPO_4$; this phase is consistent with observed and predicted $REPO_4$ transformation pathways.

Keywords: high pressure; rare earth orthophosphate; phase transformation; X-ray diffraction

Citation: Sharma, J.; Packard, C.E. Uncovering the Effects of Non-Hydrostaticity on Pressure-Induced Phase Transformation in Xenotime-Structured $TbPO_4$. *Solids* **2024**, *5*, 110–122. https://doi.org/10.3390/solids5010008

Academic Editor: Sophie Guillemet-Fritsch

Received: 4 January 2024
Revised: 6 February 2024
Accepted: 11 February 2024
Published: 16 February 2024

1. Introduction

The deformation mechanisms of rare earth orthophosphates ($REPO_4$s) under complex stress states are highly pertinent to several research fields including geoscience and structural ceramics. In shocked xenotime and monazite minerals, $REPO_4$ deformation microstructures can provide insight into the extreme conditions generated during impact events [1–3]. In addition, the pressure-induced xenotime–monazite phase transformation of certain $REPO_4$ compositions offers the possibility of enhanced toughness and plasticity in ceramic matrix composites (CMCs) for aerospace components subject to extreme conditions [4,5]. When tested as CMC fiber coatings, transforming compositions have been shown to deflect or arrest cracks and facilitate fiber sliding at lower stresses than non-transforming compositions [5].

Identifying $REPO_4$ compositions that undergo the pressure-induced xenotime–monazite phase transformation requires understanding the compositional phase boundary in the middle of the lanthanide series. In equilibrium at 1 atm (10^{-4} GPa), compositions with smaller RE^{3+} ionic radii (RE = Tb—Lu, Sc, Y) adopt the xenotime (tetragonal, $I4_1/amd$) structure while those with larger RE^{3+} ionic radii (RE = La-Gd) adopt the monazite (monoclinic, $P2_1/n$) structure [6]. Under high hydrostatic pressure, xenotime-structured compositions are known to transform into either the monazite structure or the scheelite (tetragonal, $I4_1/a$) structure, with the latter being more favorable in xenotime compositions with the smallest RE^{3+} ionic radii [7]. The three aforementioned crystal structures are illustrated in Figure 1.

The xenotime, monazite, and scheelite structures all contain chains of alternating RE-O polyhedra and PO_4 tetrahedra and have RE-O coordination numbers of 8, 9, and 8, respectively [8]. Figure 1 shows the compaction of the $REPO_4$ structure from xenotime to monazite to scheelite due to the increasing rotations and translations of the RE-O polyhedra and PO_4

tetrahedra [8]. Such rotations and translations can be induced using hydrostatic pressure, and they can be prematurely induced in the presence of non-hydrostatic stress, which disrupts stable bonding symmetries more dramatically than pure hydrostatic stress [5,9]. An intermediate structure, anhydrite (orthorhombic, Amma), has also been reported in xenotime compositions that are extremely close to the xenotime–monazite phase boundary (e.g., $Gd_{0.5}Tb_{0.5}PO_4$) or subjected to high deviatoric stresses at low hydrostatic pressures (e.g., $Gd_xDy_{1-x}PO_4$, $TbPO_4$) [5,10,11].

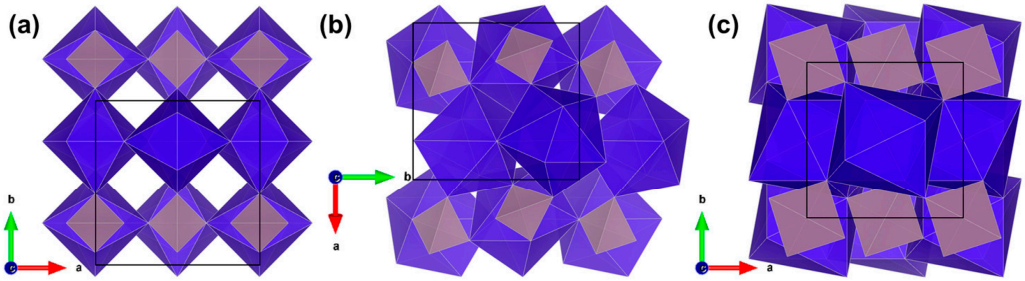

Figure 1. [001] views of $REPO_4$ structure in the (**a**) xenotime, (**b**) monazite, and (**c**) scheelite phases. RE-O polyhedra are shown in violet, PO_4 tetrahedra are shown in grey, and the unit cell boundaries are shown as thin black boxes. The 90° rotation of monazite axes with respect to those of xenotime and scheelite is a result of the monoclinic cell setting of monazite, as shown in the detailed transformation schemes reported by Hay et al. [5]. Figure adapted from Sharma et al. [7].

While the pressure-induced phase transformations of $REPO_4$s have been extensively characterized in (quasi-)hydrostatic environments via in situ diamond anvil cell (DAC) X-ray diffraction (XRD) and Raman spectroscopy (RS), studies which systematically evaluate the influence of non-hydrostaticity are extremely limited [7]. Such studies typically vary the pressure-transmitting medium (PTM) in the DAC in order to vary the hydrostaticity of the stress state experienced by the sample. For example, Santamaria-Perez et al. studied orthorhombic $BaSO_4$ using three different fluid PTMs (helium, silicone oil, and 4:1 methanol–ethanol), finding a decreasing hydrostatic limit led to lower transformation onset pressures (P_{onset}) and wider pressure ranges of phase coexistence [12]. In $REPO_4$ literature specifically, Lacomba-Perales et al.'s in situ DAC XRD study notes that shear promotes earlier xenotime–monazite transformation in YPO_4, but this conclusion is based on a cursory comparison of their findings to a prior YPO_4 study carried out by others [13]. Our recent in situ DAC XRD study probed the effect of shear on the xenotime–monazite transformation of $DyPO_4$ by systematically varying the PTM [9]. We found neon and 16:3:1 methanol–ethanol–water (MEW) PTM yield similar P_{onset} values of 9.1(1) GPa and 9.3 GPa, respectively, while KCl PTM yields a much lower P_{onset} of 7.0 GPa (a ~22% drop). Even though neon crystallizes at 4.7 GPa, neon and MEW both remain (quasi-)hydrostatic at P_{onset}; therefore, employing only one of these two PTMs is sufficient (assuming other conditions are held constant) [14]. The significant P_{onset} reduction under KCl is likely attributable to a higher shear stress state given the fact that KCl is never hydrostatic, and its ambient pressure bulk modulus (B_0) is ~20 times that of neon [15–17]. We note that B_0 does not reflect the DAC conditions at P_{onset} since a material's bulk modulus (B) generally increases with pressure. However, materials whose B_0 values differ by orders of magnitude do not attain similar B values at the high pressures of interest. At a given DAC pressure, an increase in the B value of a PTM results in less PTM compression, which is expected to generate greater contact stresses and friction at PTM–sample interfaces. Given the non-uniform magnitude and direction of the contact stresses and friction, greater shear stress is expected to be induced in the sample. While the quantification of stress transfer and shear stress generation by solid PTMs has not been detailed in the literature, results from prior DAC experiments on α-Ti support the expectation that solid PTMs with higher B_0 impart more shear stress on the sample than PTMs with lower B_0 [18]. Because $DyPO_4$ was not tested under any solid PTM (solid at 1 atm) other than KCl, another high-shear state was

not evaluated. Beyond our $DyPO_4$ study, the effect of shear on phase transformations has yet to be reported for any other $REPO_4$ [9]. In addition, the high-pressure, post-monazite phase of $TbPO_4$ has yet to be experimentally observed.

This study employs in situ DAC synchrotron XRD to probe the pressure-induced phase transformations of xenotime $TbPO_4$ under variable hydrostaticity. The experiments performed in this study involve three PTMs: neon, KCl, and "none" (i.e., cell packed with sample and no PTM material). In the "none" PTM condition, the sample is effectively the PTM. Xenotime $DyPO_4$ is also tested in the "none" condition to build on our prior study [9]. $DyPO_4$ and $TbPO_4$ have B_0 values of 144 GPa and 134 GPa, respectively, which are an order of magnitude higher than the B_0 of KCl [9,19]. Our $TbPO_4$ experiment using neon PTM shows a xenotime–monazite P_{onset} of 8.7(6) GPa, which is lower than other reported XRD-based hydrostatic P_{onset} values of 9.8 GPa and 9.9 GPa [19]. In addition, $TbPO_4$ experiments in this study show a systematic lowering of the xenotime–monazite P_{onset} when changing the PTM from neon to KCl to "none" (i.e., as PTM bulk modulus increases). Lastly, our $TbPO_4$ experiment with no medium shows an almost 50% drop in P_{onset} (reaching the lowest value reported for any $REPO_4$ to date), provides evidence for scheelite as the post-monazite phase, and corroborates Hay et al.'s ex situ observation of monazite in indented xenotime $TbPO_4$.

2. Materials and Methods

Xenotime $TbPO_4$ and $DyPO_4$ powders were synthesized via precipitation reactions and subsequent calcination. Details of these synthesis steps are provided in the Supplementary Materials. The sample powder consisted of grains ranging from sub-micrometer to a few micrometers in size; these grains exhibited the anisotropic, elongated crystal habit expected of tetragonal materials (see Figure S1). In situ DAC XRD was conducted at room temperature at Beamline 12.2.2 of the Advanced Light Source at Berkeley National Laboratory. For experiments involving neon PTM, DACs were loaded with neon using the University of Chicago Gas Loader in the high-pressure lab at Beamline 12.2.2. Two-dimensional diffraction patterns were collected with a PILATUS 3S 1M detector at an X-ray wavelength of 0.4947 Å and an exposure time of 20 s. All DACs used were of the symmetric Princeton design and were compressed using a membrane driven by a Druck PACE 6000 pressure controller. Additional experiment details are shown in Table 1. In the table and elsewhere in the manuscript, values within parentheses following a pressure represent the standard deviation of the last digit of the pressure.

Table 1. Details of the XRD experiments performed at Beamline 12.2.2 at the Advanced Light Source.

Experiment Name	Sample	PTM	Culet Diameter (μm)	Spot Size (μm)	Gasket Material	Gasket Indented Thickness, Hole Diameter (μm)	P_{max} (GPa)
Tb-neon	$TbPO_4$	neon	500	30	301 stainless steel	60–80, 260	14.0(10)
Tb-KCl	$TbPO_4$	KCl	500	20	301 stainless steel	60–80, 260	11.9(8)
Tb-none	$TbPO_4$	none	300	10	rhenium	50, 160	19.3(14)
Dy-none	$DyPO_4$	none	300	30	rhenium	50, 160	10.4(7)

For pressure marking during initial membrane engagement, ruby was used (R1 fluorescence calibration) [20], while gold was used during diffraction data collection (using a 3rd order Birch–Murnaghan equation of state) [21]. Data collection began at pressures higher than 0 GPa due to some initial compression required to confirm membrane engagement. There are no reported $TbPO_4$ or $DyPO_4$ phase transitions below these starting pressures (as corroborated by prior work); therefore, the initial jump does not preclude any material insight [7,9,19]. The maximum pressure in each experiment (P_{max}) was limited by the performance of the gasket. Experiments were concluded when the gasket hole collapsed, approached the edge of the culets, or was otherwise unable to maintain a proper seal.

XRD pattern integration, masking, and background subtraction were performed using Dioptas [22]. Pattern fitting was then performed using X'Pert HighScore Plus 3.0 [23]. This software fits monazite using the $P2_1/c$ cell setting as a default. Though both the $P2_1/c$ and $P2_1/n$ cell settings are valid descriptions of monazite (space group No. 14), fitted lattice parameters were converted to the $P2_1/n$ cell setting to facilitate comparison to the literature. The LeBail fitting approach was used instead of traditional Rietveld structural refinement to accommodate the significant preferred orientation present in all scans [24]. This apparent preferred orientation appears due to the small spot size of the beam with respect to the grain size of the sample (effectively sampling a finite number of grains), rather than any systematic preferred orientation of the sample grains. P_{onset} is determined by visual inspection of individual XRD patterns and fit residuals, not by judging color in the contour plots shown in the next section. Visual inspection involves plotting the square root of intensity against Q to ensure emerging peaks are not overlooked due to their extremely low intensity. The following reference structures were used in this study: xenotime $TbPO_4$ from Lopez-Solano et al. [19], xenotime $DyPO_4$ from Milligan et al. [25], monazite $TbPO_4$ and $DyPO_4$ from Heuser et al. [26], anhydrite $TbPO_4$ from Losch et al. [27], gold from Couderc et al. [28], ruby from Jephcoat et al. [29], and calculated scheelite $TbPO_4$ from López-Solano et al. [19]. In the XRD patterns, the peaks of the ruby, anhydrite $TbPO_4$, and scheelite $TbPO_4$ structures are extremely weak or obscured by stronger peaks; as a result, LeBail fits incorporating these phases did not converge. Thus, the peaks of these three phases were only used in peak position comparison and were not employed in LeBail fitting. Traces of the anhydrite phase of $TbPO_4$ appear at the beginning of the Tb-neon experiment and may have arisen inadvertently from grinding during sample preparation or DAC loading. This phase does not appear in every scan (or even in every experiment), as the particular set of sample grains under X-ray illumination varies. For computation involving derived data (e.g., unit cell volume, gold-based pressure, cell setting conversion), the uncertainties Python package was used to propagate error [30].

3. Results and Discussion

Across all experiments, increasing pressure causes XRD peaks to drift to higher Q and broaden due to uniform and non-uniform strain, respectively. In addition, XRD signal quality deteriorates under increasingly non-hydrostatic PTMs (i.e., going from neon to KCl to none); this trend has been previously reported in hydrostaticity studies of other materials [12,18]. Given these effects, the XRD patterns analyzed in the current study are limited to pressures at which key peaks are sufficiently distinguishable for phase identification and LeBail fitting.

For the Tb-neon experiment, Figure 2a shows XRD pattern evolution throughout the entire experiment, while Figure 2b shows LeBail fit quality at $P_{initial}$ (1.6(1) GPa), P_{onset} (8.7(6) GPa), the transformation end pressure (P_{end}, 13.7(10) GPa), and P_{max} (14.0(10) GPa). The first scan in this experiment features xenotime, anhydrite, and gold (upward triangle symbol) peaks. At ~5 GPa, the neon PTM crystallizes, and conditions shift from hydrostatic (in liquid neon) to quasi-hydrostatic (in solid neon) [31]. Solid neon adopts an FCC structure and is still extremely compressible with a bulk modulus of ~1 GPa [32]. Neon remains the most compressible material in the DAC, as evidenced by neon peaks shifting much more dramatically with increasing pressure than the other materials' peaks in Figure 2a. The first discernible monazite peaks emerge at 8.7(6) GPa and are located at Q = 1.58 $Å^{-1}$, 1.59 $Å^{-1}$, 1.98 $Å^{-1}$, 2.13 $Å^{-1}$, and 2.29 $Å^{-1}$ (as denoted by stars in Figure 2); these are the (110), (10$\bar{2}$), (002), (02$\bar{1}$), and (21$\bar{2}$) reflections, respectively. Figure 2 also shows these peaks grow with pressure. In the P_{onset} scan in Figure 2b, the refined monazite lattice parameters are a = 6.175(1) Å, b = 6.699(1) Å, c = 6.483(1) Å, and β = 100.67(1)°. This P_{onset} value is higher than neon's crystallization pressure and lower than neon's hydrostatic limit, meaning the stress state is quasi-hydrostatic at P_{onset}. With increasing pressure, monazite peaks grow while xenotime peaks diminish. At 13.7(10) GPa, there are no longer any clearly discernible peaks that are attributable to xenotime. Therefore, 13.7(10) GPa is P_{end} and

yields a xenotime–monazite phase coexistence range of 5.0(10) GPa. In the final scan at 14.0(10) GPa, monazite, gold, and neon are the only phases present.

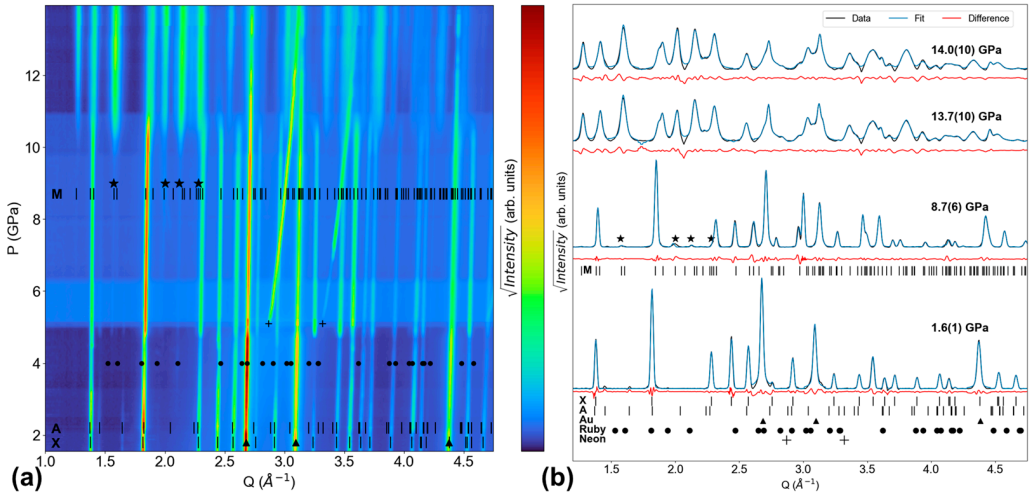

Figure 2. Tb-neon XRD experiment. (**a**) Contour plot of all XRD patterns. (**b**) Select XRD patterns (initial, onset of monazite, end of xenotime, final) and their LeBail fits. Monazite peaks emerge at 8.7(6) GPa. 'X', 'M', and 'A' ticks show $TbPO_4$ peak positions for the xenotime [25], monazite [26], and anhydrite phases [27], respectively. Triangles, circles, pluses, and stars denote the peak positions of gold [28], ruby [29], neon [31], and emerging monazite, respectively.

A key result from the Tb-neon experiment is the P_{onset} of 8.7(6) GPa, which is the lowest P_{onset} value for $TbPO_4$ in neon PTM reported to date. Lopez-Solano et al. reported a higher value of 9.9 GPa based on XRD experiments also conducted with neon PTM [19]. Our experiment shows monazite peaks are clear at 9.9 GPa and at pressures leading up to this value (see Figure 2a). Figure 3 provides a closer look at our dataset, showing how including the monazite structure improves the fit of the XRD pattern collected at 8.7(6) GPa.

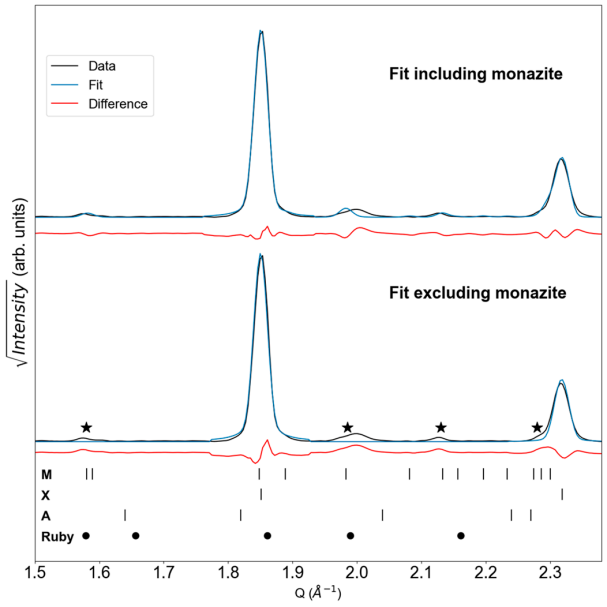

Figure 3. LeBail fits with and without monazite for the P_{onset} scan from the Tb-neon experiment. 'X', 'M', and 'A' ticks show $TbPO_4$ peak positions for the xenotime [25], monazite [26], and anhydrite [27] phases, respectively. Circles show reference ruby peak positions [29], and stars indicate regions of intensity consistent with monazite peaks.

When monazite is excluded from the fit, there are regions of increased residual intensity (denoted by stars) that align with monazite peak positions. Although some ruby peaks are also quite close to the starred regions, ruby peaks do not align with all of these regions. Furthermore, the ruby signal is not expected to intensify with pressure, while the intensity in those starred regions does (as shown in Figure 2).

Further consideration of thermodynamic data between neighboring $REPO_4$ compounds gives additional support to a lower P_{onset} than the one reported by Lopez-Solano et al. [19]. Thermodynamic data (i.e., calculated enthalpy differences between xenotime and monazite phases as well as experimental calcination temperatures required to convert monazite to xenotime) show the monazite phase is more favorable in $TbPO_4$ than in $DyPO_4$ [33–36]. As a result, $TbPO_4$ is expected to have a lower xenotime–monazite P_{onset} than $DyPO_4$, but Lopez-Solano et al.'s $TbPO_4$ P_{onset} is higher than the previously reported $DyPO_4$ P_{onset} of 9.1(1) GPa (also in neon PTM) [9]. The lower $TbPO_4$ P_{onset} reported in the present study is consistent with thermodynamic expectations. Nevertheless, the P_{end} of 13.7(10) GPa determined in this study is consistent with Lopez-Solano et al.'s P_{end} of 13.8 GPa.

For the Tb-KCl experiment, Figure 4a shows XRD pattern evolution throughout the entire experiment, while Figure 4b shows LeBail fit quality at $P_{initial}$ (2.2(2) GPa), P_{onset} (5.6(4) GPa), and P_{max} (11.9(8) GPa). The first scan in this experiment contains peaks belonging to xenotime, gold (upward triangle symbol), and B1-KCl (left-pointing triangle symbol). B1-KCl is the ambient pressure phase of KCl with a NaCl-type structure, and it begins transforming into the CsCl-type B2-KCl structure (right-pointing triangle symbol) at 2.3(1) GPa. Similar to neon in the Tb-neon experiment, KCl in this experiment is the most compressible material in the DAC, causing its peaks to shift in Q more than the sample's peaks [37]. KCl peaks do not shift as dramatically as neon's peaks in the Tb-neon experiment because KCl has a higher bulk modulus than neon.

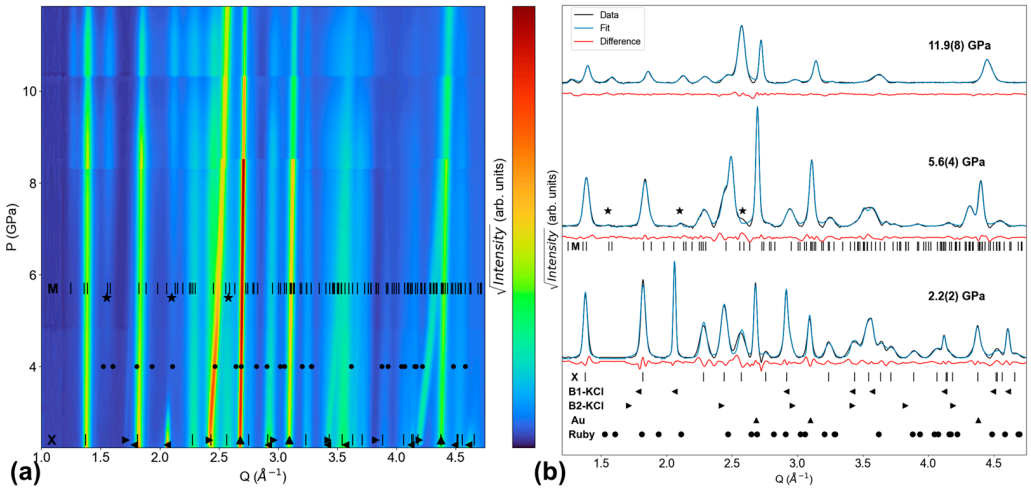

Figure 4. Tb-KCl XRD experiment. (**a**) Contour plot of all XRD patterns. (**b**) Select XRD patterns (initial, onset of monazite, final) and their LeBail fits. Monazite peaks emerge at 5.6(4) GPa. 'X' and 'M' ticks show $TbPO_4$ peak positions for the xenotime and monazite phases, respectively [25,26]. Circles, upward triangles, left-pointing triangles, right-pointing triangles, and stars denote the peak positions of ruby [29], gold [28], B1-KCl [37], B2-KCl [37], and emerging monazite, respectively.

At 5.6(4) GPa, monazite peaks emerge at Q = 1.55 $Å^{-1}$, 2.1 $Å^{-1}$, and 2.58 $Å^{-1}$ (as denoted by stars in Figure 4); these are the (110), $(02\bar{1})$, and (211) reflections, respectively. In the P_{onset} scan, the refined monazite lattice parameters are a = 6.239(1) Å, b = 6.832(3) Å, c = 6.793(1) Å, and β = 99.06(1)°. Both the xenotime and monazite phases persist through the end of the experiment at 11.9(8) GPa, so the phase coexistence range is at least

6.3(8) GPa. In the final scan at 11.9(8) GPa, xenotime, monazite, gold, and B2-KCl are the only phases present.

For the Tb-none experiment, Figure 5a shows XRD pattern evolution throughout the entire experiment, while Figure 5b shows LeBail fit quality at $P_{initial}$ (1.9(1) GPa), the xenotime–monazite P_{onset} (4.4(3) GPa), the potential scheelite P_{onset} (10.2(7) GPa), and P_{max} (19.3(14) GPa). The first scan in this experiment shows xenotime, gold (upward triangle symbol), and possibly weak ruby (circle symbol) peaks. At 4.4(3) GPa, monazite peaks emerge at Q = 1.55 $Å^{-1}$, 2.10 $Å^{-1}$, and 2.58 $Å^{-1}$ (as denoted by stars in Figure 5); these are the (110), (02$\bar{1}$), and (211) reflections, respectively. In the P_{onset} scan, the refined monazite lattice parameters are a = 6.134(1) Å, b = 6.870(1) Å, c = 6.187(2) Å, and β = 99.83(2)°.

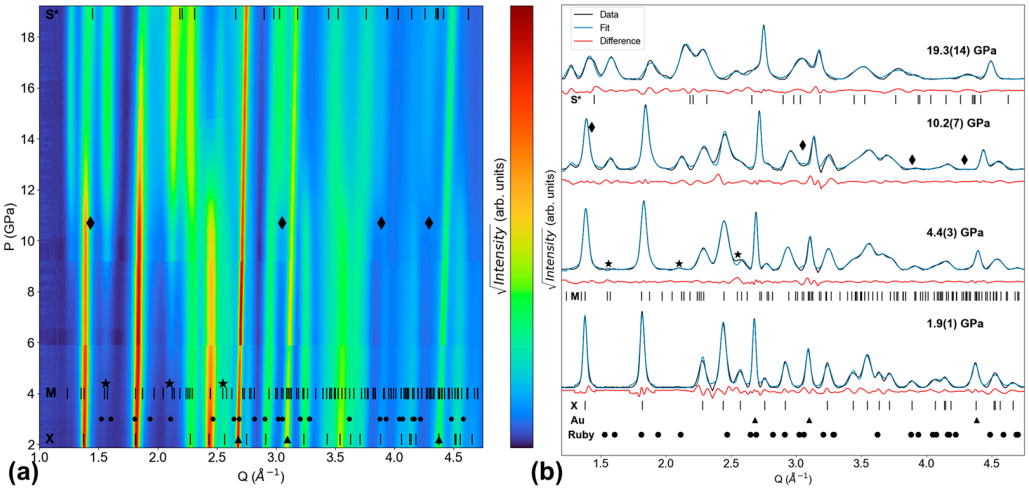

Figure 5. Tb-none XRD experiment. (**a**) Contour plot of all XRD patterns. (**b**) Select XRD patterns (initial, onset of monazite, onset of scheelite, final) and their LeBail fits. Monazite peaks emerge at 4.4(3) GPa. Scheelite peaks appear to emerge at 10.2(7) GPa. 'X', 'M', and 'S*' ticks show $TbPO_4$ peak positions for the xenotime [19], monazite [26], and scheelite (simulated at 20.5 GPa) phases [19], respectively. Triangles, circles, stars, and diamonds denote the peak positions of gold [28], ruby [29], emerging monazite, and emerging scheelite, respectively.

At 10.2(7) GPa, new peaks emerge at Q = 1.43 $Å^{-1}$, 3.05 $Å^{-1}$, 3.89 $Å^{-1}$, and 4.29 $Å^{-1}$ (denoted by diamond symbols in Figure 5), and these peaks grow as pressure continues to increase. The phase giving rise to these peaks is likely scheelite-structured $TbPO_4$, as Lopez-Solano et al. and Bose et al. both predicted scheelite would be the post-monazite phase of $TbPO_4$, and scheelite has been experimentally observed in YPO_4, $TmPO_4$, $YbPO_4$, $LuPO_4$, and $ScPO_4$ [19,38–40]. Figure 5 also shows 'S*' ticks, which represent the peak positions of a scheelite $TbPO_4$ structure simulated at 20.5 GPa, as reported by Lopez-Solano et al. [19]. The diamond symbols are not perfectly aligned with the S* ticks; however, this slight misalignment is expected given the differences in conditions between this experimental study and Lopez-Solano et al.'s simulation (e.g., pressure, stress state, temperature, and the confounding effects of these factors on individual peak positions). Therefore, the emergence of new peaks (diamond symbols) and their proximity to the 'S*' ticks suggests the presence of scheelite is plausible and requires confirmation via further XRD experiments. If confirmed, 10.2(7) GPa would be the lowest pressure at which any scheelite structure has been reported in $REPO_4$s to date.

The final scan in this experiment contains xenotime, monazite, gold, and potentially scheelite. Therefore, this experiment yields a xenotime–monazite phase coexistence range of at least 14.9(14) GPa and a potential xenotime–monazite–scheelite phase coexistence range of at least 9.1(14) GPa.

A Dy-none experiment was also performed to build on our prior $DyPO_4$ study, in which KCl was the only PTM tested that was solid at 1 atm [9]. Figure 6a shows XRD

pattern evolution throughout the entire experiment, while Figure 6b shows LeBail fit quality at $P_{initial}$ (3.1(2) GPa), at the xenotime–monazite P_{onset} (6.9(5) GPa), and at P_{max} (10.4(7) GPa). The first scan in this experiment shows xenotime, gold (upward triangle symbol), and ruby (circle symbol) peaks. At 6.9(5) GPa, monazite peaks emerge at Q = 1.59 $Å^{-1}$, 2.10 $Å^{-1}$, and 2.57 $Å^{-1}$ (as denoted by stars in Figure 5); these are the (110), (02$\bar{1}$), and (211) reflections, respectively. In the P_{onset} scan, the refined monazite lattice parameters are a = 6.187(3) Å, b = 6.603(2) Å, c = 6.783(5) Å, and β = 102.40(4)°. The final scan at 10.4(7) GPa contains xenotime, monazite, and gold. Consequently, the $DyPO_4$ xenotime–monazite phase coexistence range is found to be at least 3.5(7) GPa.

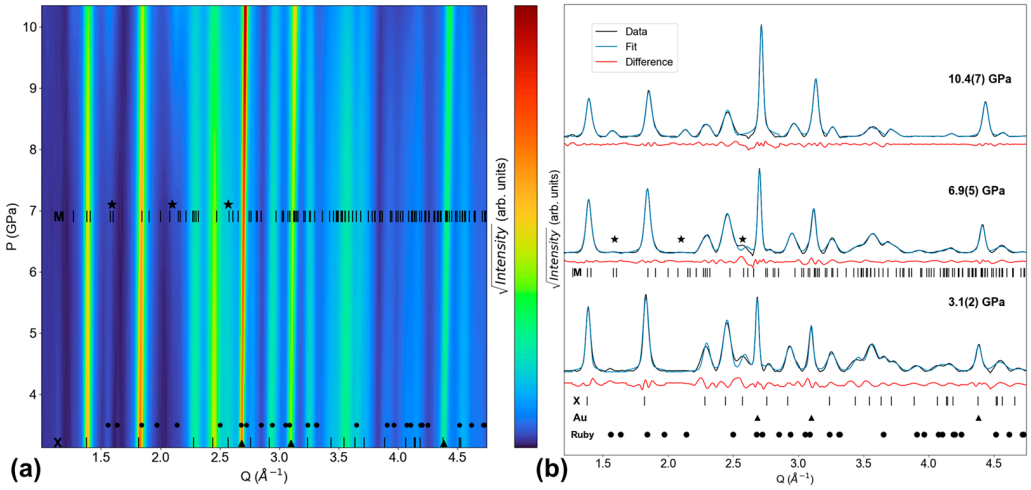

Figure 6. Dy-none XRD experiment. (**a**) Contour plot of all XRD patterns. (**b**) Select XRD patterns (initial, onset of monazite, final) and their LeBail fits. Monazite peaks emerge at 6.9(5) GPa. 'X' and 'M' ticks show $DyPO_4$ peak positions for the xenotime and monazite phases, respectively [25,26]. Triangles, circles, and stars denote the peak positions of gold [28], ruby [29], and emerging monazite, respectively.

Figure 7 summarizes the $DyPO_4$ and $TbPO_4$ phase behavior transformation data reported in this study as well as in two prior $DyPO_4$ studies [7,9]. In the $DyPO_4$ section, phase data from an experiment using the MEW PTM (Dy-MEW [7]) are shown, since a prior experiment using neon (Dy-neon [9]) did not reach pressures high enough to gauge the xenotime–monazite phase coexistence range. MEW has a hydrostatic limit of 10.5(5) GPa and is therefore hydrostatic at the xenotime–monazite P_{onset}, like neon. The P_{onset} from the Dy-neon experiment (9.1(1) GPa) is shown as an orange dashed line in Figure 7 and is within the error bar of the P_{onset} from the Dy-MEW experiment (9.6(7) GPa).

Figure 7 shows $DyPO_4$ and $TbPO_4$ both exhibit xenotime–monazite P_{onset} reductions with non-hydrostatic PTMs. Shear can facilitate the plastic deformation involved in phase transformation (i.e., polyhedral rotations and translations) and thereby reduce the hydrostatic pressure required to induce phase transformation. In fact, non-hydrostatic conditions have been suggested to lower the pressure required to induce mechanical instability in other $REPO_4$ and $REVO_4$ materials [41,42]. High-pressure dynamical instability (i.e., the softening of Raman-active and silent phonon modes) has also been observed in these materials, but it has less influence on P_{onset} than mechanical instability does [36,41,42]. In addition, the $TbPO_4$ P_{onset} values are marginally (KCl) or significantly (none) lower than those of $DyPO_4$ in the same PTM. $TbPO_4$ P_{onset} values being lower likely stems from the monazite phase being more thermodynamically favorable in $TbPO_4$ than in $DyPO_4$ regardless of the kinetic barriers involved [33–36].

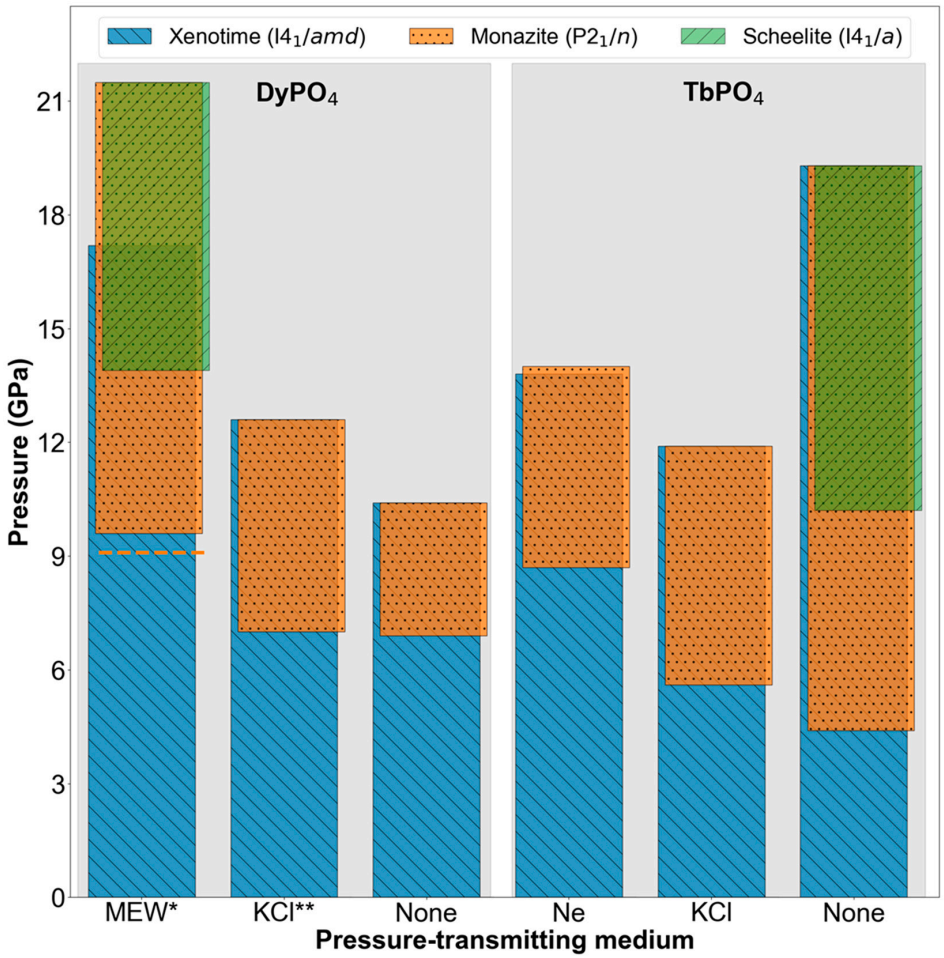

Figure 7. High-pressure XRD-based phase map of $DyPO_4$ and $TbPO_4$, each tested with three different PTMs. The legend lists the phases with their corresponding space groups. For each $REPO_4$-PTM combination, the upper limit of the highest bar(s) represents the highest pressure at which data are reported and does not represent a phase boundary. * The Dy-MEW data were originally reported by Sharma et al. [7]. The dashed orange line shows the $DyPO_4$ xenotime–monazite P_{onset} value using neon PTM [9]. ** The Dy-KCl data were originally reported by Sharma et al. [9].

Figure 7 also shows the onset of the scheelite phase at 13.9(10) GPa in the Dy-MEW experiment and at 10.2(7) GPa in the Tb-none experiment. This difference in scheelite P_{onset} values is likely a convolution of compositional and shear effects. Because the Tb-none experiment is less hydrostatic than the Dy-MEW experiment, the onset pressure of the scheelite phase in the former experiment is expected to be lower. This expectation is consistent with observations from the other experiments. However, the effect of composition on the onset of the scheelite phase remains unclear. Moreover, the lack of scheelite (green bars) in the other four experiments shown in Figure 7 may simply be a consequence of those four experiments not reaching sufficiently high pressures. Considering strictly the $DyPO_4$ experiments, we expect the scheelite P_{onset} to be lower in Dy-KCl and Dy-none than in Dy-MEW (as MEW is the most hydrostatic medium of the three) based on a hypothesis of shear-induced lowering of transformation pressure. Unfortunately, the Dy-KCl and Dy-none experiments terminated at pressures significantly lower than the scheelite P_{onset} of Dy-MEW, leaving significant untested pressure ranges in which the onset of scheelite is still plausible. Considering the $TbPO_4$ experiments, the emergence of scheelite in Tb-none evidently shows a shear-induced lowering of P_{onset} because scheelite is not observed at the same pressure in lower shear experiments (i.e., Tb-neon, Tb-KCl). These lower shear experiments are expected to yield higher scheelite P_{onset} values than Tb-none, so the lack

of scheelite observation may be attributable to an insufficient P_{max}. In order to clarify the presence of scheelite, additional Dy-KCl, Dy-none, Tb-neon, and Tb-KCl experiments going to higher pressures are merited.

Next, the effect of shear on xenotime–monazite phase coexistence is considered. All experiments shown in Figure 7 show significant phase coexistence ranges of at least 3 GPa, further supporting the notion that $REPO_4$ phase transformations are diffusional rather than martensitic. Consistent with our prior $DyPO_4$ studies, the coexistence of multiple $REPO_4$ phases at certain pressures defies Gibbs' phase rule and further shows the sluggish nature of pressure-induced phase transformation in these materials [7,9]. Furthermore, the $TbPO_4$ experiments show that while shear induces earlier onset of transformation, it does not induce earlier completion of transformation. While the xenotime–monazite coexistence range is 5.0(10) GPa in the Tb-neon experiment, this range extends to at least 6.3(8) GPa and at least 14.9(14) GPa in the Tb-KCl and Tb-none experiments, respectively. This range extension has also been reported in $BaSO_4$ and α-Ti when these materials are compressed using non-hydrostatic PTMs [18,19]. At a fundamental level, extended phase coexistence under shear may be attributable to non-uniform stress fields causing varying degrees of transformation progression in a given volume of material. Conclusions regarding coexistence trends cannot be drawn from the $DyPO_4$ experiments, as the Dy-KCl and Dy-none experiments do not go to sufficiently high pressures. For completeness, plots showing the pressure-dependence of $TbPO_4$ and $DyPO_4$ monazite and xenotime lattice parameters as well as a table of axial compressibilities are provided in the Supplementary Materials.

The findings in this study provide key insights for understanding $REPO_4$s under complex stress states and inform potential structural applications, including CMC fiber coatings. This work provides in situ evidence to corroborate ex situ observations of phase transformation of $TbPO_4$ under shear from other types of experiments (e.g., indentation, fiber pull-out) [4,5]. In addition, this study shows a high-shear environment can lower the P_{onset} to pressures below the xenotime $REPO_4$'s hardness, suggesting transformation-related strain-hardening affects measured hardness values [4,43]. Moreover, this work suggests $REPO_4$ compositions further from the xenotime–monazite phase boundary (i.e., with higher hydrostatic P_{onset} values) may be considered for CMC fiber coating applications if P_{onset} is proven to drop as dramatically under shear as it does in $TbPO_4$. The benefits of $REPO_4$ phase transformation (i.e., enhanced CMC plasticity and toughening) may be accessible at lower pressures and over a wider range of pressures than previously understood.

4. Conclusions

This study systematically probes the effect of non-hydrostaticity on the pressure-induced phase transformations of xenotime $TbPO_4$ using in situ DAC XRD. Our prior $DyPO_4$ study found non-hydrostatic KCl PTM induces the xenotime–monazite phase transformation at a pressure ~22% lower than in hydrostatic media (e.g., neon, 16:3:1 MEW) [9]. In this work, our experiments with three PTMs (neon, KCl, and none) show a lowering of the $TbPO_4$ xenotime–monazite P_{onset} from 8.7(6) GPa to 5.6(4) GPa to 4.4(3) GPa, respectively. The P_{onset} value for $TbPO_4$ with no PTM is the lowest value reported to date for any $REPO_4$ and represents an almost 50% P_{onset} reduction in a high-shear stress state relevant to potential CMC applications. When comparing $DyPO_4$ and $TbPO_4$, the latter's P_{onset} values are consistently lower; this fact is likely due to the monazite phase being more thermodynamically favorable in $TbPO_4$ than in $DyPO_4$. Lastly, our $TbPO_4$ experiment with no PTM provides preliminary proof of scheelite as the high-pressure, post-monazite phase.

Supplementary Materials: The following supporting information can be downloaded at: https://www.mdpi.com/article/10.3390/solids5010008/s1. Details of sample powder synthesis; Figure S1: Scanning electron micrograph and energy-dispersive X-ray spectrum of $TbPO_4$ sample powder; Figures S2–S5: Plots showing the pressure dependence of xenotime and monazite lattice parameters

from the Tb-neon, Tb-KCl, Tb-none, and Dy-none experiments. Table S1 shows axial compressibilities of lattice parameters from all experiments. Table S2 shows R-values of LeBail fits from Figures 2b, 4b, 5b and 6b. Table S3 shows bulk modulus values obtained from 3rd order Birch-Murnaghan equation of state fits.

Author Contributions: Conceptualization, J.S. and C.E.P.; data curation, J.S. and C.E.P.; formal analysis, J.S.; writing—original draft preparation, J.S.; writing—review and editing, J.S. and C.E.P.; supervision, C.E.P. All authors have read and agreed to the published version of the manuscript.

Funding: This research was supported by the National Science Foundation under Award No. DMR-1352499. J.S. was supported by the Department of Defense through the National Defense Science & Engineering Graduate Fellowship Program. This work was performed at Beamline 12.2.2, Advanced Light Source, Berkeley National Laboratory. Beamline 12.2.2 is partially supported by COMPRES, the Consortium for Materials Properties Research in Earth Sciences under NSF Cooperative Agreement EAR 1606856. The Advanced Light Source is supported by the Director, Office of Science, Office of Basic Energy Sciences, U.S. Department of Energy under Contract No. DE-AC02-05CH11231.

Data Availability Statement: All relevant data that support the findings of this study are available from the corresponding authors upon request.

Acknowledgments: This work was performed at Beamline 12.2.2, Advanced Light Source, Berkeley National Laboratory. The authors thank the beamline scientists: Martin Kunz, Kathrin Armstrong, and Bora Kalkan. The authors also greatly appreciate the assistance of John Copley and Tom Duffy at Princeton University in providing diamond anvil cells and invaluable support while preparing for and performing experiments. In addition, the authors thank Ivar Reimanis for lending his diamond anvil cell for beamline experiments. Moreover, the authors thank Henry Afful for helping perform experiments as well as Matthew Musselman for synthesizing the $DyPO_4$ sample. This research was supported by the National Science Foundation under Award No. DMR-1352499. J.S. was supported by the Department of Defense through the National Defense Science & Engineering Graduate Fellowship Program. Beamline 12.2.2 is partially supported by COMPRES, the Consortium for Materials Properties Research in Earth Sciences under NSF Cooperative Agreement EAR 1606856. Beamline 12.2.2 at the Advanced Light Source is a DOE Office of Science User Facility under contract no. DE-AC02-05CH11231.

Conflicts of Interest: The authors declare no conflict of interest.

References

1. Seydoux-Guillaume, A.M.; de Resseguier, T.; Montagnac, G.; Reynaud, S.; Leroux, H.; Reynard, B.; Cavosie, A.J. Bridging the Shocked Monazite Gap—Deformation Microstructures in Natural and Laser Shock-Loaded Samples. *Earth Planet. Sci. Lett.* **2022**, *595*, 117727. [CrossRef]
2. Cox, M.A.; Cavosie, A.J.; Poelchau, M.; Kenkmann, T.; Bland, P.A.; Miljković, K. Shock Deformation Microstructures in Xenotime from the Spider Impact Structure, Western Australia. In *Large Meteorite Impacts and Planetary Evolution VI*; Geological Society of America: Boulder, CO, USA, 2021; pp. 449–464.
3. Erickson, T.M.; Timms, N.E.; Pearce, M.A.; Cayron, C.; Deutsch, A.; Keller, L.P.; Kring, D.A. Shock-Produced High-Pressure (La, Ce, Th)PO_4 Polymorph Revealed by Microstructural Phase Heritage of Monazite. *Geology* **2019**, *47*, 504–508. [CrossRef]
4. Hay, R.S.; Boakye, E.E.; Mogilevsky, P.; Fair, G.E.; Parthasarathy, T.A.; Davis, J.E. Transformation Plasticity in $(Gd_xDy_{1-x})PO_4$ Fiber Coatings During Fiber Push Out. *J. Am. Ceram. Soc.* **2013**, *96*, 1586–1595. [CrossRef]
5. Hay, R.S.; Mogilevsky, P.; Boakye, E. Phase Transformations in Xenotime Rare-Earth Orthophosphates. *Acta Mater.* **2013**, *61*, 6933–6947. [CrossRef]
6. Ni, Y.; Hughes, J.M.; Mariano, A.N. Crystal Chemistry of the Monazite and Xenotime Structures. *Am. Mineral.* **1995**, *80*, 21–26. [CrossRef]
7. Sharma, J.; Afful, H.Q.; Packard, C.E. Phase Transformation Pathway of $DyPO_4$ to 21.5 GPa. *Crystals* **2023**, *13*, 249. [CrossRef]
8. Macey, B.J. *The Crystal Chemistry of MTO_4 Compounds with the Zicron, Scheelite, and Monazite Structure Types*; Virginia Tech: Blacksburg, VA, USA, 2009.
9. Sharma, J.; Musselman, M.; Haberl, B.; Packard, C.E. In Situ Synchrotron Diffraction of Pressure-Induced Phase Transition in $DyPO_4$ under Variable Hydrostaticity. *Phys. Rev. B* **2021**, *103*, 184105. [CrossRef]
10. Tschauner, O.; Ushakov, S.V.; Navrotsky, A.; Boatner, L.A. Phase Transformations and Indications for Acoustic Mode Softening in Tb-Gd Orthophosphate. *J. Phys. Condens. Matter* **2016**, *28*, 035403. [CrossRef] [PubMed]
11. Lösch, H.; Hirsch, A.; Holthausen, J.; Peters, L.; Neumeier, S.; Huittinen, N. *Site-Selective Fluorescence Spectroscopy Investigations of $LnPO_4$ Xenotime Ceramics for Radioactive Waste Disposal*; HZDR: Dresden, Germany, 2016; Volume 13.

12. Santamaría-Pérez, D.; Gracia, L.; Garbarino, G.; Beltrán, A.; Chuliá-Jordán, R.; Gomis, O.; Errandonea, D.; Ferrer-Roca, C.; Martínez-García, D.; Segura, A. High-Pressure Study of the Behavior of Mineral Barite by X-ray Diffraction. *Phys. Rev. B.* **2011**, *84*, 054102. [CrossRef]
13. Lacomba-Perales, R.; Errandonea, D.; Meng, Y.; Bettinelli, M. High-Pressure Stability and Compressibility of APO_4 (A=La, Nd, Eu, Gd, Er, and Y) Orthophosphates: An X-ray Diffraction Study Using Synchrotron Radiation. *Phys. Rev. B.* **2010**, *81*, 064113. [CrossRef]
14. Klotz, S.; Chervin, J.-C.; Munsch, P.; Le Marchand, G. Hydrostatic Limits of 11 Pressure Transmitting Media. *J. Phys. D Appl. Phys.* **2009**, *42*, 075413. [CrossRef]
15. Uts, I.; Glazyrin, K.; Lee, K.K.M. Effect of Laser Annealing of Pressure Gradients in a Diamond-Anvil Cell Using Common Solid Pressure Media. *Rev. Sci. Instrum.* **2013**, *84*, 103904. [CrossRef] [PubMed]
16. Dewaele, A.; Datchi, F.; Loubeyre, P.; Mezouar, M. High Pressure-High Temperature Equations of State of Neon and Diamond. *Phys. Rev. B* **2008**, *77*, 094106. [CrossRef]
17. Dewaele, A.; Belonoshko, A.B.; Garbarino, G.; Occelli, F.; Bouvier, P.; Hanfland, M.; Mezouar, M. High-Pressure-High-Temperature Equation of State of KCl and KBr. *Phys. Rev. B* **2012**, *85*, 214105. [CrossRef]
18. Errandonea, D.; Meng, Y.; Somayazulu, M.; Häusermann, D. Pressure-Induced $\alpha \rightarrow \omega$ Transition in Titanium Metal: A Systematic Study of the Effects of Uniaxial Stress. *Phys. B Condens. Matter* **2005**, *355*, 116–125. [CrossRef]
19. López-Solano, J.; Rodríguez-Hernández, P.; Muñoz, A.; Gomis, O.; Santamaría-Perez, D.; Errandonea, D.; Manjón, F.J.; Kumar, R.S.; Stavrou, E.; Raptis, C. Theoretical and Experimental Study of the Structural Stability of $TbPO_4$ at High Pressures. *Phys. Rev. B* **2010**, *81*, 144126. [CrossRef]
20. Shen, G.; Wang, Y.; Dewaele, A.; Wu, C.; Fratanduono, D.E.; Eggert, J.; Klotz, S.; Dziubek, K.F.; Loubeyre, P.; Fat'yanov, O.V.; et al. Toward an International Practical Pressure Scale: A Proposal for an IPPS Ruby Gauge (IPPS-Ruby2020). *High Press. Res.* **2020**, *40*, 299–314. [CrossRef]
21. Anderson, O.L.; Isaak, D.G.; Yamamoto, S. Anharmonicity and the Equation of State for Gold. *J. Appl. Phys.* **1989**, *65*, 1534–1543. [CrossRef]
22. Prescher, C.; Prakapenka, V.B. DIOPTAS: A Program for Reduction of Two-Dimensional X-ray Diffraction Data and Data Exploration. *High Press. Res.* **2015**, *35*, 223–230. [CrossRef]
23. Degen, T.; Sadki, M.; Bron, E.; König, U.; Nénert, G. The High Score Suite. *Powder Diffr.* **2014**, *29*, S13–S18. [CrossRef]
24. Le Bail, A. Whole Powder Pattern Decomposition Methods and Applications: A Retrospection. *Powder Diffr.* **2005**, *20*, 316–326. [CrossRef]
25. Milligan, W.O.; Mullica, D.F.; Beall, G.W.; Boatner, L.A. The Structures of Three Lanthanide Orthophosphates. *Inorganica Chim. Acta* **1983**, *70*, 133–136. [CrossRef]
26. Heuser, J.M.; Neumeier, S.; Peters, L.; Schlenz, H.; Bosbach, D.; Deissmann, G. Structural Characterisation of Metastable Tb- and Dy-Monazites. *J. Solid State Chem.* **2019**, *273*, 45–52. [CrossRef]
27. Lösch, H.; Hirsch, A.; Holthausen, J.; Peters, L.; Xiao, B.; Neumeier, S.; Schmidt, M.; Huittinen, N. A Spectroscopic Investigation of Eu^{3+} Incorporation in $LnPO_4$ (Ln = Tb, $Gd_{1-X}Lu_X$, X = 0.3, 0.5, 0.7, 1) Ceramics. *Front. Chem.* **2019**, *7*, 94. [CrossRef]
28. Couderc, J.J.; Garigue, G.; Lafourcade, L.; Nguyen, Q.T. Standard X-Ray Diffraction Powder Patterns. *Z. Met.* **1959**, *50*, 708–716.
29. Jephcoat, A.P.; Hemley, R.J.; Mao, H.K. X-ray Diffraction of Ruby (Al_2O_3:Cr^{3+}) to 175 GPa. *Phys. B+C* **1988**, *150*, 115–121. [CrossRef]
30. Lebigot, E.O. Welcome to the Uncertainties Package—Uncertainties Python Package 3.0.1 Documentation. Available online: https://pythonhosted.org/uncertainties/ (accessed on 4 January 2024).
31. Hemley, R.J.; Zha, C.S.; Jephcoat, A.P.; Mao, H.K.; Finger, L.W.; Cox, D.E. X-ray Diffraction and Equation of State of Solid Neon to 110 GPa. *Phys. Rev. B* **1989**, *39*, 11820–11827. [CrossRef] [PubMed]
32. Finger, L.W.; Hazen, R.M.; Zou, G.; Mao, H.K.; Bell, P.M. Structure and Compression of Crystalline Argon and Neon at High Pressure and Room Temperature. *Appl. Phys. Lett.* **1981**, *39*, 892–894. [CrossRef]
33. Ushakov, S.V.; Helean, K.B.; Navrotsky, A.; Boatner, L.A. Thermochemistry of Rare-Earth Orthophosphates. *J. Mater. Res.* **2001**, *16*, 2623–2633. [CrossRef]
34. Ji, Y.; Kowalski, P.M.; Kegler, P.; Huittinen, N.; Marks, N.A.; Vinograd, V.L.; Arinicheva, Y.; Neumeier, S.; Bosbach, D. Rare-Earth Orthophosphates From Atomistic Simulations. *Front. Chem.* **2019**, *7*, 436276. [CrossRef] [PubMed]
35. Mogilevsky, P. On the Miscibility Gap in Monazite-Xenotime Systems. *Phys. Chem. Miner.* **2007**, *34*, 201–214. [CrossRef]
36. Musselman, M.A.; Wilkinson, T.M.; Haberl, B.; Packard, C.E. In Situ Raman Spectroscopy of Pressure-Induced Phase Transformations in Polycrystalline $TbPO_4$, $DyPO_4$, and $Gd_xDy_{(1-x)}PO_4$. *J. Am. Ceram. Soc.* **2018**, *101*, 2562–2570. [CrossRef]
37. Froyen, S.; Cohen, M.L. Structural Properties of Nacl and Kc1 under Pressure. *J. Phys. C Solid State Phys.* **1986**, *19*, 2623–2632. [CrossRef]
38. Bose, P.P.; Mittal, R.; Chaplot, S.L.; Loong, C.K.; Boatner, L.A. Inelastic Neutron Scattering, Lattice Dynamics, and High-Pressure Phase Stability of Zircon-Structured Lanthanide Orthophosphates. *Phys. Rev. B.* **2010**, *82*, 094309. [CrossRef]
39. Zhang, F.X.; Wang, J.W.; Lang, M.; Zhang, J.M.; Ewing, R.C.; Boatner, L.A. High-Pressure Phase Transitions of $ScPO_4$ and YPO_4. *Phys. Rev. B.* **2009**, *80*, 184114. [CrossRef]
40. Zhang, F.X.; Lang, M.; Ewing, R.C.; Lian, J.; Wang, Z.W.; Hu, J.; Boatner, L.A. Pressure-Induced Zircon-Type to Scheelite-Type Phase Transitions in $YbPO_4$ and $LuPO_4$. *J. Solid State Chem.* **2008**, *181*, 2633–2638. [CrossRef]

41. Gomis, O.; Lavina, B.; Rodríguez-Hernández, P.; Muñoz, A.; Errandonea, R.; Errandonea, D.; Bettinelli, M. High-Pressure Structural, Elastic, and Thermodynamic Properties of Zircon-Type $HoPO_4$ and $TmPO_4$. *J. Phys. Condens. Matter* **2017**, *29*, 095401. [CrossRef]
42. Marqueño, T.; Errandonea, D.; Pellicer-Porres, J.; Santamaría-Pérez, D.; Rodríguez-Hernández, P.; Muñoz, A. Competing Dynamical and Lattice Instabilities in RVO_4 Rare-Earth Vanadium Oxides under High Pressure. *Phys. Rev. Mater.* **2022**, *6*, L060601. [CrossRef]
43. Wilkinson, T.M.; Wu, D.; Musselman, M.A.; Li, N.; Mara, N.; Packard, C.E. Mechanical Behavior of Rare-earth Orthophosphates near the Monazite/Xenotime Boundary Characterized by Nanoindentation. *Mater. Sci. Eng. A* **2017**, *691*, 203–210. [CrossRef]